 doi:10.20944/preprints202104.0696.v1

Article

Combining Satellite InSAR, Slope Units and Finite Element Modeling for Stability Analysis in Mining Waste Disposal Areas

Juan López-Vinielles [1,2,3,*], José A. Fernández-Merodo [1,4], Pablo Ezquerro [1,2], Juan C. García-Davalillo [1], Roberto Sarro [1], Cristina Reyes-Carmona [1], Anna Barra [5], José A. Navarro [5], Vrinda Krishnakumar [5], Massimiliano Alvioli [6] and Gerardo Herrera [1,7]

[1] Geohazards InSAR Laboratory and Modelling Group (InSARlab), Geoscience Research Department, Geological Survey of Spain (IGME), Calle de Ríos Rosas 23, 28003 Madrid, Spain; jose.fernandez@igme.es (J.A.F.-M.); p.ezquerro@igme.es (P.E.); jc.garcia@igme.es (J.C.G.-D.); r.sarro@igme.es (R.S.); c.reyes@igme.es (C.R.-C.); g.herrera@igme.es (G.H.)
[2] Escuela Técnica Superior de Ingenieros de Caminos, Canales y Puertos, Universidad Politécnica de Madrid, Calle Profesor Aranguren s/n, 28040 Madrid, Spain
[3] HEMAV SL, Carrer d'Esteve Terrades 1, 08860 Castelldefels, Spain
[4] Escuela Técnica Superior de Ingenieros de Minas y Energía, Universidad Politécnica de Madrid, Calle Ríos Rosas 21, 28003, Madrid, Spain
[5] Division of Geomatics, Centre Tecnològic de Telecomunicacions de Catalunya (CTTC/CERCA), Avinguda Carl Friedrich Gauss 7, 08860 Castelldefels, Spain; abarra@cttc.cat (A.B.); jose.navarro@cttc.es (J.A.N.); vrinda.krishnakumar@cttc.cat (V.K.)
[6] Consiglio Nazionale delle Ricerche, Istituto di Ricerca per la Protezione Idrogeologica, Via Madonna Alta 126, I-06128 Perugia, Italy; massimiliano.alvioli@irpi.cnr.it (M.A.)
[7] EuroGeoSurveys: Earth Observation and Geohazards Expert Group (EOEG), Rue Joseph II 36-38, 1000 Brussels, Belgium
* Correspondence: juan.lopezv@alumnos.upm.es (J.L.-V.)

Abstract: Slope failures pose a substantial threat to mining activity due to their destructive potential and high probability of occurrence on steep slopes close to limit equilibrium conditions, often found both in open pits and in waste and tailing disposal facilities. The development of slope monitoring and modeling programs usually entails the exploitation of in situ and remote sensing data together with the application of numerical modeling, and it plays an important role in the definition of prevention and mitigation measures aimed at minimizing the impact of slope failures in mining areas. Here we present a new methodology combining satellite radar interferometry and 2D finite element modeling for slope stability analysis at a regional scale, applied within slope unit polygons. We studied a former mining area in southeast Spain, and the method proved useful in detecting and characterizing a considerably large number of unstable slopes. Out of 1,959 slope units used for the spatial analysis of the radar interferometry data, 43 were unstable, with varying values of safety factor and landslide size. Out of the 43 active slope units, 21 exhibited line of sight velocities greater than the maximum error obtained through the validation analysis (2.5 cm/year). Eventually, this work discusses the possibility of using the results of the proposed approach to devise a proxy for landslide hazard. The proposed methodology can help to provide non-expert final users with intelligible, clear and easily comparable information to analyze slope instabilities in different settings, not limited to mining areas.

Keywords: Satellite radar interferometry (InSAR); Slope units; Active deformation slope units; Finite element method (FEM); Shear strength reduction (SSR); Slope stability; Abandoned mining areas.

1. Introduction

Mining activities frequently induce ground movements for different reasons. In underground mining, instability normally develops as a consequence of adverse structural

 doi:10.20944/preprints202104.0696.v1

geology, substantial stress, weathering and/or softening of rocks, and excessive groundwater pressure or flow [1]. Such conditions may lead to the collapse of underground openings. All of these factors can give rise, in turn, to ground subsidence. In surface mining, instability is generally the result of exposure of dominant weakness planes, although failure through intact rock is also possible in very weak rocks and formations. It mainly affects excavated slopes and may result in catastrophic events if appropriate measures to prevent slope failure are not undertaken. Slope instability often affects waste and tailing disposal facilities as well, essential in both surface and underground mining operations. These facilities consist of unconsolidated debris material arranged in waste dumps and tailing dams.

Slope failures and subsidence can cause serious problems such as environmental impacts, damage to property, harm to the health and safety of both employees and residents of nearby communities, and economic outcomes that can either result in a premature closure of the mine [2], or compromise the reclamation and decommissioning of the mining operation. Both phenomena may occur long after the mine workings have been abandoned [3]. Moreover, unlike civil engineering projects where the useful and expected life of the structures is very long—more than 10 years, mining projects only require certain facilities to have long lives (*e.g.* shafts, main haulage drifts, etc.).

For this reason, the safety factor (*SF*) used in the design of mining structures is much lower than that used in civil structures and, in many situations, a $SF \approx 1$ is used [2]. Low *SF*s do not imply, however, that safety is less important in mining. Rather, profit margins are narrow and the total costs must be kept to a minimum. In all mining operations, it is always a major challenge for the designers to ensure the integrity and stability of all openings and excavations while keeping the costs low. Yet in most mining projects, investing in specific ground monitoring programs early can produce major cost savings in the future. A clear example would be the case of large open-pit mines where the slopes are designed and allowed to move in order to reduce the amount of waste to be mined while monitoring the movements very carefully.

In order to ensure a safe and stable condition, ground monitoring in mining has been traditionally undertaken through the application of surface and subsurface techniques [4]. Recently, the development of modern monitoring systems such as time domain reflectometers (TDR) [5], terrestrial laser scanners (TLS) [6], radars (*e.g.* GB-SAR, SSR and MSR) [7–9], and unmanned aerial vehicles (UAV) [10,11], motivated a rise in the use of remote sensing technologies. All of the mentioned methods require, however, in situ measurements for calibration and validation, and in some cases represent a costly solution.

Application of satellite Synthetic Aperture Radar Interferometry (InSAR) [12] has been used as a supplementary technique to study mining-induced ground movements. As in the case of other remote sensing techniques, InSAR results require validation of the measured ground movements, typically carried out using in situ monitoring data. In addition, they can be used in conjunction with numerical models reproducing the measured movements after ground truth verification [13–15].

In particular, case studies on the use of satellite InSAR to analyze mining-induced slope instabilities are scarce, as most of them focus on ground subsidence [*e.g.* 16–18]. Although such application has been documented in a few mining sites at Australia [19,20], Brazil [21,22], Spain [23,24], South Africa [15], Turkey [7] and U.S.A. [14,25]. Most of the cases either present analyses of the InSAR data at slope scale or include no complementary stability analyses taking into account geotechnical data through geo-mechanical modeling.

Here, we propose a topography-driven methodology to analyze slope instabilities at a regional scale using satellite InSAR in conjunction with 2D finite element (FE) modeling. The method is topography-driven because it makes use of slope units (SUs) as mapping units, instead of the widely used grid cells. SUs are portions of geomorphologically homogeneous terrain. The proposed approach aims to simplify the InSAR- and FE-modeling-derived results in order to provide non-expert final users with intelligible, clear and easily comparable information.

Preprints (www.preprints.org) | NOT PEER-REVIEWED | Posted: 26 April 2021 doi:10.20944/preprints202104.0696.v1

The methodology has been implemented for the region of Sierra de Cartagena-La Unión (Murcia), hereinafter referred to as Sierra Minera, a former mining area in southeast Spain (Figure 1). The literature contains a few case studies conducted in Sierra Minera through satellite InSAR. However, most of them focus on mapping and monitoring ground subsidence within the urban area of La Unión [26,27]—no longer occurring in the area according to our InSAR data.

One of the existing studies mapped ground movements in Sierra Minera using satellite InSAR [23]. Yet the data used in that study were obtained by processing ERS and ENVISAT satellite data. Hence, the spatial resolution of the results (80 by 80 m) and the density of measuring points (MPs) were rather low.

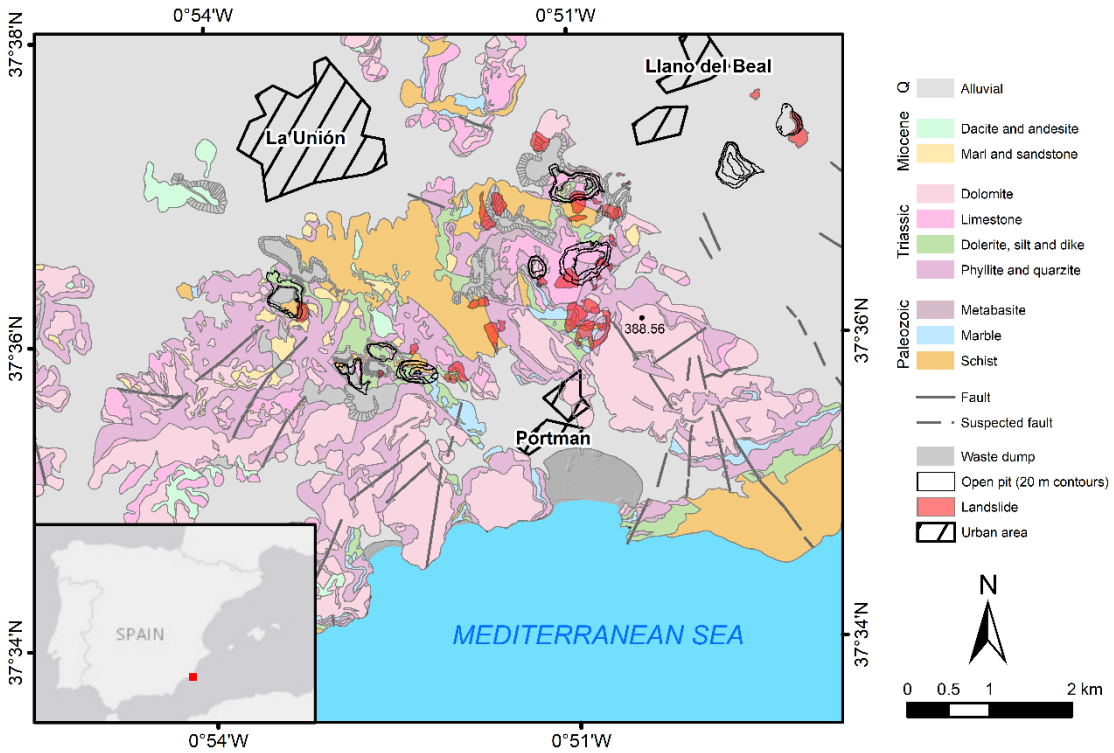

Figure 1. Study area and geological map of Sierra de Cartagena-La Unión (adapted from [28]).

In contrast, our results have been obtained by processing Sentinel-1 satellite data. Thus, we derived line-of-sight (LOS) ground velocity maps over Sierra Minera at a higher resolution (30 by 30 m) and with a much higher density of MPs. This improvement is not only due to higher spatial resolution of the Sentinel-1 constellation, but to its short revisit time (6 days). In addition, we performed stability analyses through 2D FE modeling to cross-reference the InSAR data.

The proposed approach builds upon previously published works aimed at detecting active deformation areas [29–32]. In these studies, however, the topography is only taken into account to discern flat areas from hill slopes—the concept of SU is not considered, and no stability analyses are performed. Moreover, whereas these studies are conceived to analyze ground deformation phenomena in general, our approach focuses exclusively on analyzing slope instability.

The paper is organized as follows. Section 2 provides an overview of the geographical, geological and geotechnical characteristics of Sierra Minera, as well as a summary of the data used for this study, some of which were collected through fieldwork. Section 3 includes a detailed explanation of the different steps of the proposed approach. Section 4 describes and discusses the obtained results. Eventually, Section 5 summarizes the main findings, and draws conclusions of this study.

Preprints (www.preprints.org) | NOT PEER-REVIEWED | Posted: 26 April 2021 doi:10.20944/preprints202104.0696.v1

2. Study area and data

2.1. Geological, lithological and geotechnical setting

The study area is located in Sierra Minera, at a distance of approximately 50 km south-southeast from the city of Murcia, at the south-easternmost part of Spain (Figure 1). The region extends over an area of 50 km^2, with a maximum elevation of 389 m a.s.l. at Peña del Águila. It is limited by the Mediterranean Sea to the south, and by the Campo de Cartagena basin to the north.

Sierra Minera contains one of the largest Pb and Zn ore deposits in the south of Europe [33], which has been exploited from the Iberian period until 1991 [34]. It is a coastal mountain range with an approximate east-west trend, that belongs to the Internal Zones of the Betic Cordillera.

The Betic Cordillera, an Alpine chain that acquired its present configuration during the Neogene, was developed from late Mesozoic to Cenozoic with the convergence between the African and Iberian plates [35]. The Internal Zones comprise three complex nappes with decreasing metamorphism grade from the lower complex to the upper. These are, from bottom to top, the Nevado Filábride, the Alpujárride and the Maláguide complexes [35].

The Nevado-Filábride is mainly constituted by graphite schists, quartzitic schists, micaschists, marbles and quartzites of Paleozoic to Permo-Triassic age. Its thickness exceeds 500 m. Discordantly overlaying this complex is the Alpujárride complex, constituted by a detritic formation (epimetamorphic rocks, quartzites and phyllites) of Permian age, and by a Triassic carbonate series containing intrusive bodies of diabases and dolerites [33]. Its thickness is approximately 400 m. After a significant erosive phase, these formations were covered by the Maláguide complex, made up of a post-orogenic, Neogene series of sedimentary rocks (sandstone, quartzite, silt, limestone and conglomerate) [36]. An important fracturation phase followed, during which uplift due to intrusive magmatism from Miocene—evidenced by sub-volcanic and volcanic outcrops, gave rise to the present-day relief. Finally, a thin level of quaternary alluvial deposits, formed by sand, silt and clays, overlies the complex nappes.

Two important fault systems, north-70 and north-130, developed between the Eocene and Middle Miocene period. These systems control the magmatic outcrops and formed the present horst and graben geologic setting of Sierra Minera bedrock [33]. Pumping tests carried out in well points over the study area revealed that most of the lithologies are fairly impermeable (*e.g.* those formed by schists, phyllites and marls) [28]. Yet quaternary formations, Miocene sedimentary rocks and some Alpujárride detritic units are permeable.

The mineralization is mainly constituted by two sulphide deposits on the carbonated sequences in the Nevado-Filábride and Alpujárride complexes. It is characterized by a strict stratigraphic control, although many faults are also mineralized and sometimes contain thick seams. In addition, the mineralization can also be found disseminated in Miocenic materials, gossans, stockworks and veins [33].

The deposits were mainly exploited through underground mining using the room-and-pillar method until the decade of the 1960s, when large open-pit exploitations were developed. One third of the total reserves was extracted between 1940 and 1990, thanks to the application of differential flotation processes and open-pit mining [33].

Over the years, 12 open pits were excavated, 3,000 wells were drilled, and hundreds of galleries and waste dumps were developed [36]. The waste dump debris material was dumped on existing hillsides without any particular safety measures, remaining in a limit equilibrium situation ($SF \approx 1$).

The first ecological restoration in Sierra Minera was conducted in 1982 by Peñarroya SA, the mining company. It was carried out by sealing the mining tailings with a soil layer in order to allow the colonization by the vegetation and avoid mobilization of heavy metals [37]. Thereafter, in 1996, the Spanish Geological Survey conducted an environmental

Preprints (www.preprints.org) | NOT PEER-REVIEWED | Posted: 26 April 2021 doi:10.20944/preprints202104.0696.v1

restoration project aimed at characterizing the geo-mechanical properties of dominant lithologies in the area (Table 1) [28]. For this purpose, geotechnical boreholes, as well as in situ and laboratory tests, were carried out. The study concluded that the presence of schists, phyllites and, most importantly, waste dump debris material, favored the occurrence of slope instabilities. Moreover, it was found that these instabilities were induced by intense and short periods of rainfall triggering torrential events. In Sierra Minera, these type of events are concentrated in a few days along the year—20 or 30, mainly in autumn. In this paper we provide insight into the analysis of such slope instabilities.

Table 1. Geo-mechanical properties of dominant lithologies [28].

Lithology	Density [kgm^{-3}]	Saturated density [kgm^{-3}]	Young modulus [kNm^{-2}]	Poisson ratio	Friction angle [°]	Cohesion [kNm^{-2}]
Graphite schists	$2.60 \cdot 10^3$	$2.63 \cdot 10^3$	$3.0 \cdot 10^5$	0.3	31	160
Mica-schists	$2.40 \cdot 10^3$	$2.43 \cdot 10^3$	$3.0 \cdot 10^5$	0.3	30	100
Phyllites	$2.20 \cdot 10^3$	$2.21 \cdot 10^3$	$3.0 \cdot 10^5$	0.3	25	86
Waste dump debris	$2.00 \cdot 10^3$	$2.00 \cdot 10^3$	$4.5 \cdot 10^4$	0.3	20	100

2.2. In situ and satellite data

For the purpose of landslide mapping and monitoring, in situ investigations were conducted over the study area through geomorphic analysis and topographic surveying. A landslide inventory (Figure 1) was elaborated through fieldwork and aerial-photo interpretation, updating previously published data [23]. Most of the inventoried landslides affect waste dump areas and open-pit slopes. Yet some landslides, associated with the presence of phyllites and schists, seem to affect both cut and fill slopes from haul roads. Most of the mapped slope instabilities can be classified as complex movements, frequently consisting of debris roto-translational landslides, debris flows, and translational landslides together with rockfalls and toppling [38].

In addition, in situ topographic surveying activities were performed using Differential Global Positioning System (DGPS) instrumentation. Thus, ground monitoring data were obtained for validation purposes from two campaigns performed in 11 July 2017 and 15 November 2018 over one of the inventoried landslides.

In view of the conducted in situ monitoring campaigns, two stacks with 64 and 83 Sentinel-1 Single Look Complex (SLC) images (spatial resolution of 3 by 14 m), respectively acquired under ascending and descending passes, were considered for the investigation, covering the period from 10 July 2017 to 15 November 2018. Finally, we used a Digital Elevation Model (DEM) of the study area with spatial resolution of 5 by 5 m, corresponding to December 2009 acquisitions, downloaded from the National Geographic Institute of Spain [39].

3. Methodology

The methodology presented herein relies on the joint exploitation of remote sensing, in situ and additional available data, to quantify mean LOS ground velocity, 2D safety factor *SF* and 2D landslide size *LS*, for a set of automatically-mapped slope instabilities. It essentially comprises three successive steps. First, we derived LOS ground velocity maps using a web-based unsupervised satellite InSAR processing chain, which we validate with DGPS data. Then, we performed a spatial analysis of the InSAR-retrieved velocities exploiting an optimized SU map, from which we obtained an active deformation slope unit (ADSU) map. Finally, we use 2D FE modeling to perform stability analyses on each ADSU from the optimal map. As a result, we estimate for each ADSU, its LOS ground velocity (V_{LOS}), its safety factor *SF* and its (landslide) size *LS* (Figure 2). The results can be updated, for a continuous assessment, by repeating the analysis on a regular basis.

Preprints (www.preprints.org) | NOT PEER-REVIEWED | Posted: 26 April 2021 doi:10.20944/preprints202104.0696.v1

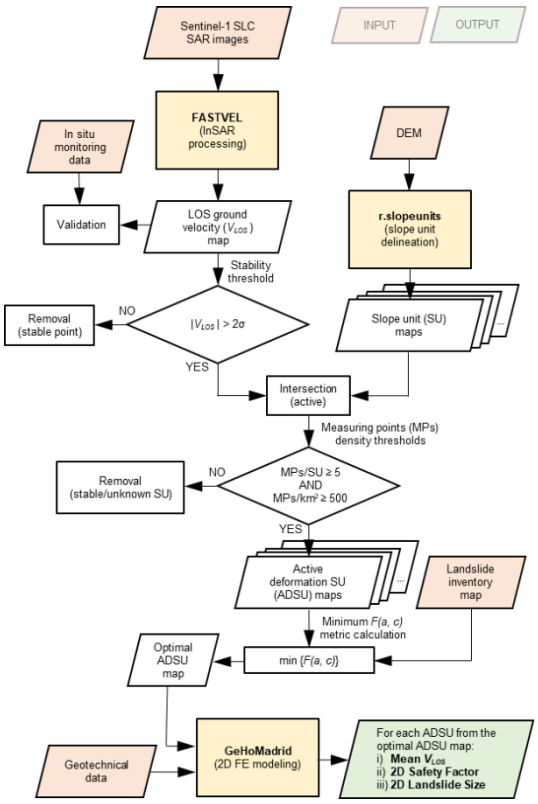

Figure 2. Flowchart of the proposed methodology.

The input data needed to apply the proposed methodology include a stack of SAR images, a DEM, a landslide inventory map, a geotechnical map, and in situ ground monitoring data for validation.

The automatic mapping procedure is based on the aggregation of the active MPs within the boundaries of different sets of morphological SUs, with varying sizes. In fact, SUs can be delineated requiring different degrees of aspect homogeneity, resulting in different maps containing a varying number of polygons.

An ADSU map is obtained for each SU delineation. The different ADSU maps are evaluated to find the map best matching the landslides observed in the study area. We refer to the best matching map as the optimal ADSU map. ADSUs are used to derive 2D cross-sections also following an automatic procedure. Finally, stability analyses are performed for each cross-section taking into account their geo-mechanical properties.

The different steps of the methodology, as well as the results obtained at each step, are described in detail in the next sections.

3.1. Advanced differential satellite InSAR processing and comparison with in situ DGPS measurements

LOS ground velocity maps in the study area were derived by processing the aforementioned Sentinel-1 images stacks using FASTVEL [12,40], an on-demand, unsupervised processing service available on the Geohazards Exploitation Platform (GEP) [41]. GEP is part of the Thematic Exploitation Platforms (TEP) initiative set up by the European Space Agency (ESA), aiming to support the exploitation of satellite Earth Observation (EO) for geohazards assessment (https://geohazards-tep.eu/) [42,43].

FASTVEL offers two different processing modes, namely interferogram generation (IFG) and multi-temporal analysis (MTA), aimed respectively at generating differential interferograms or Persistent Scatterrer Interferometry (PSI)-based mean ground velocity maps. EO sources supported by FASTVEL include ERS, Envisat-ASAR and Sentinel-1.

Preprints (www.preprints.org) | NOT PEER-REVIEWED | Posted: 26 April 2021 doi:10.20944/preprints202104.0696.v1

In MTA mode, the service provides the following output results: (i) a LOS ground velocity map, (ii) the updated topography, including a reference DEM with height uncertainty, and (iii) a CSV file with the main LOS PSI products. Once the SAR images over the area of interest are selected, few processing parameters are requested to the user, providing some default values if preferred. These account for the maximum temporal and spatial baseline, the maximum Doppler centroid difference, the maximum image Doppler centroid value, and the Goldstein phase filter exponential factor. In addition, the user must select a mean coherence threshold to set the initial grid of points, and a maximum Atmospheric Phase Screen (APS) correlation distance for linking the initially selected points to minimize APS propagation. For a detailed description of the FASTVEL service, please refer to its user guide [44].

In this study, default values were adopted for most of the parameters. Thus, LOS ground velocity maps could be calculated in the study area both in ascending and descending geometry for the period monitored by DGPS.

Then, the DGPS ground velocities were projected onto the LOS for comparison, considering both geometries (ascending and descending), using the following equations:

$$V_{LOS}^{GPS} = V_{3D}^{GPS} \cdot \cos\theta, \tag{1}$$

$$\cos\theta = cosE_{3D}^{GPS} \cdot \cos\alpha_{LOS}^{SAR} \cdot \cos\beta_{LOS}^{SAR} + cosN_{3D}^{GPS} \cdot \sin\alpha_{LOS}^{SAR} \cdot \cos\beta_{LOS}^{SAR} + cosU_{3D}^{GPS} \cdot \sin\beta_{LO} \tag{2}$$

$$\alpha_{LOS}^{SAR} = \tan^{-1}\frac{cosN_{LOS}^{SAR}}{cosE_{LOS}^{SAR}}, \tag{3}$$

$$\beta_{LOS}^{SAR} = \tan^{-1}\frac{cosU_{LOS}^{SAR}}{\sqrt{(cosE_{LOS}^{SAR})^2+cosN_{LOS}^{SAR})^2}}. \tag{4}$$

In Eqs. (1)-(4), V_{LOS}^{GPS} and V_{3D}^{GPS} are respectively the projected and the raw ground velocities measured by DGPS, θ is the angle formed by the two velocity vectors, $cosN_{3D}^{GPS}$, $cosE_{3D}^{GPS}$ and $cosU_{3D}^{GPS}$ are respectively the north, east and up unitary vector components of the raw DGPS vector, α_{LOS}^{SAR} is the azimuth angle of the LOS vector measured on the horizontal plane from the east axis to the north axis in the counterclockwise direction, β_{LOS}^{SAR} is the incidence angle of the LOS vector measured on the vertical plane from the horizontal plane to the up axis in the counterclockwise direction, and $cosN_{LOS}^{SAR}$, $cosE_{LOS}^{SAR}$ and $cosU_{LOS}^{SAR}$ are respectively the north, east and up unitary vector components of the LOS vector.

3.2. Parametric delineation of slope units

Slope units are morphological terrain units (TUs), alternative to square grid cells, bounded by drainage and divide lines [45,46] and delineated in such a way that terrain homogeneity is maximized within the units, and inhomogeneity is maximized across neighboring units [47,48]. TUs are portions of terrain with similar geological and geomorphological features which divide a region in portions that have a set of common properties, different from the adjacent ones, across definable boundaries [49]. Thus, SUs are a particular type of TUs causally related to the hydro-geomorphological conditions [47] and represent a formalization of what geomorphologists describe as slopes.

Slope units are well suited for hydrological and geomorphological studies, and for landslide susceptibility modeling and zonation [46,50–53]. SUs are therefore particularly suited also in the context of InSAR and FE modeling, since they encompass areas with similar slope-facing direction (aspect). SUs have been used in the literature in conjunction with optical satellite imagery for landslide mapping [54]. However, the use of SUs either to aggregate InSAR data or to derive 2D FE modeling geometries has never been reported, to our knowledge.

Preprints (www.preprints.org) | NOT PEER-REVIEWED | Posted: 26 April 2021 doi:10.20944/preprints202104.0696.v1

In this work, we used the software r.slopeunits of [47] for SU delineation, freely available from http://geomorphology.irpi.cnr.it/tools/slope-units. The software is adaptive because, as outlined in [47], no unique SU delineation exists, since there is an inherent dependence on the scale and nature of the process under investigation. Given this non-univocity, the software allows SUs to be delineated with varying sizes and different degrees of homogeneity of aspect. Then, optimized SUs can be obtained by selecting the values of the software's input parameters that maximize fitness of the output SU set for a particular purpose. The input parameters required by the algorithm, their role more related to technical constraints, are described in detail in [47].

Here, the r.slopeunits software was first run multiple times with different combinations of the input parameters a (minimum area) and c (circular variance of aspect), namely a = (5,000, 10,000, 50,000, 100,000, 150,000, 250,000, 350,000, 450,000) m^2 and c = (0.01, 0.05, 0.1, 0.15, 0.25, 0.35, 0.45). Thus, we calculated 56 SU maps, corresponding to the possible (a, c) combinations. The values selected are similar to the ones used in previous works [47,55]. Flat areas were excluded from the delineation process by computing a plains map including all areas of the DEM with slope gradient lower than 5^0.

3.3. Determination of active deformation slope units

Once the 56 SU sets were obtained, the two InSAR datasets (ascending and descending) were filtered according to their standard deviations selecting only the points with $|V_{LOS}| > 2\sigma$ (*i.e.* the moving or active MPs). Then, the active MPs were superimposed to the SUs by performing the intersection of the two InSAR datasets and the 56 SU maps, amounting to 112 intersections.

We applied two different criteria to determine which SUs were active (ADSUs). Those SUs (i) containing at least five active MPs either from the ascending or descending dataset, and (ii) yielding a density of active MPs greater than or equal to 500 MPs/km^2 (around half of the maximum MPs density of FASTVEL)—from the corresponding dataset, were considered ADSUs. The two ADSU sets obtained in ascending and descending geometry for each combination of the input parameters a and c, were combined in a single set.

To select the best combination of the input parameters a and c of the r.slopeunits software, we used the error index E_I introduced by [45], also used in [54], defined as follows:

$$F(a,c) = E_I(a,c) = \frac{A_\cup(a,c) - A_\cap(a,c)}{A_\cup(a,c)}, \quad (5)$$

where $A_\cup(a,\cdot c)$ is the area of the region where either the automatically mapped ADSUs or the inventoried landslides exist (union) with the specified values of (a, c), and $A_\cap(a,\cdot c)$ is the area of the region where both exist (intersection). The optimal values of the input parameters a and c—*i.e.*, the ones corresponding to the optimal ADSU set, were obtained minimizing Eq. (5) to find the best agreement between the mapped ADSUs and the landslide inventory.

Although the optimal ADSU set was selected on the basis of the results obtained from Eq. (5), we also investigated the use of the custom metric developed in [55,56] for comparison. This metric analyzes the differences between the inventoried landslides and the predicted ones—the mapped ADSUs in this case, in terms of their cumulated frequency size distributions, and is defined as follows:

$$F(a,c) = \sqrt{\sum_{i=1}^{i=39}(D_i - P_i(a,c))^2}, \quad (6)$$

where 39 is the number of inventoried landslides, D_i is the i-th point of the distribution of the inventoried landslides and $P_i(a,c)$ is the corresponding i-th point of the distribution of the mapped ADSUs obtained with the specified values of (a, c), among the 56 different ADSU sets.

 doi:10.20944/preprints202104.0696.v1

Eventually, we discuss the results in terms of confusion matrices. The values of the confusion matrices for the two sets of ADSUs corresponding to the minimum of Eqs. (5) and (6) were further compared with the values obtained for the active deformation areas (ADAs) mapped by means of the so-called ADAFinder software package [29]. This comparison was carried out to evaluate the improvement achieved through the introduction of topographic data, since ADAFinder is an algorithm for active deformation mapping in which topography is neglected—the only input data required by the software are the InSAR-derived LOS ground velocity maps. In order to allow for a meaningful comparison, the two ADA sets obtained with ADAFinder, corresponding to ascending and descending geometry, were likewise combined in a single set.

3.4. 2D finite element modeling

Stability analyses were performed through 2D FE modeling using the shear strength reduction (SSR) technique [57,58] implemented in the GeHoMadrid code [59,60]. SSR simply reduces the soil shear strength, in terms of friction angle Φ and cohesion c, until collapse occurs. The resulting *SF* is the ratio of the soil actual shear strength to the reduced shear strength at failure.

In this work, the analyzed geometries were automatically derived from the optimal ADSU set using the centroid and the aspect values of each ADSU. Initially, three 400-m long cross-sections were derived for each ADSU considering three different aspect values that were obtained using the three most common measures of central tendency (*i.e.*, the mean, the median and the mode, the latter calculated using integer aspect values). In addition, the middle points of the profile traces of all cross-sections were fixed on the ADSUs centroids.

Then, 2D stability analyses (plane-strain conditions) were performed over the three cross-sections obtained for each ADSU, considering a single, homogeneous material and prescribing zero pore pressure on the surface, corresponding to fully saturated conditions. Different materials were assigned for each of the ADSUs, depending on the predominant lithology within their boundaries. The geo-mechanical properties of the four materials considered were taken from [28] and are listed in Table 1. For the other boundary conditions, all displacements were fixed in the bottom plane; perpendicular displacements were fixed in the lateral planes. For the applied external load, only gravity force was contemplated.

The cases in which the plastic strain contours resulting from the stability analyses did not properly fit the geometry obtained considering a length of 400 m, were repeated considering a length of 800 m. Even though most of the analyses were satisfactorily performed using either 400- or 800-m long cross-sections, a small number of cases needed to be repeated considering a length of 1,200 m. Fine meshes made up of quadratic triangular elements were used for each geometry in order to get well-defined failure mechanisms and precise *SF*s.

Once all the ADSUs were satisfactorily modeled, final results were derived from the models yielding the lowest safety factors *SF*s. In addition to the *SF*s resulting from such models, landslide sizes *LS*s were determined for each of the models by computing the surface area enclosed by the displacement contours at failure in each case. Thus, *SF*s and *LS*s could be calculated for each of the ADSUs within the optimal set.

4. Results

4.1. Ground velocity maps and validation

LOS ground velocity maps (Figure 3) revealed maximum positive LOS velocities (movement towards the satellite) of 5.8 and 8.7 cm/year respectively in ascending and descending geometry over the area of the southernmost group of inventoried landslides (Figure 1). This area also exhibited the maximum negative LOS velocity (movement away from the satellite) in descending geometry, with a value of -12.9 cm/year. The ascending

Preprints (www.preprints.org) | NOT PEER-REVIEWED | Posted: 26 April 2021 doi:10.20944/preprints202104.0696.v1

results revealed, however, a maximum negative LOS velocity of -9.9 cm/year over the area of the south-westernmost cluster of active MPs in Figure 3.

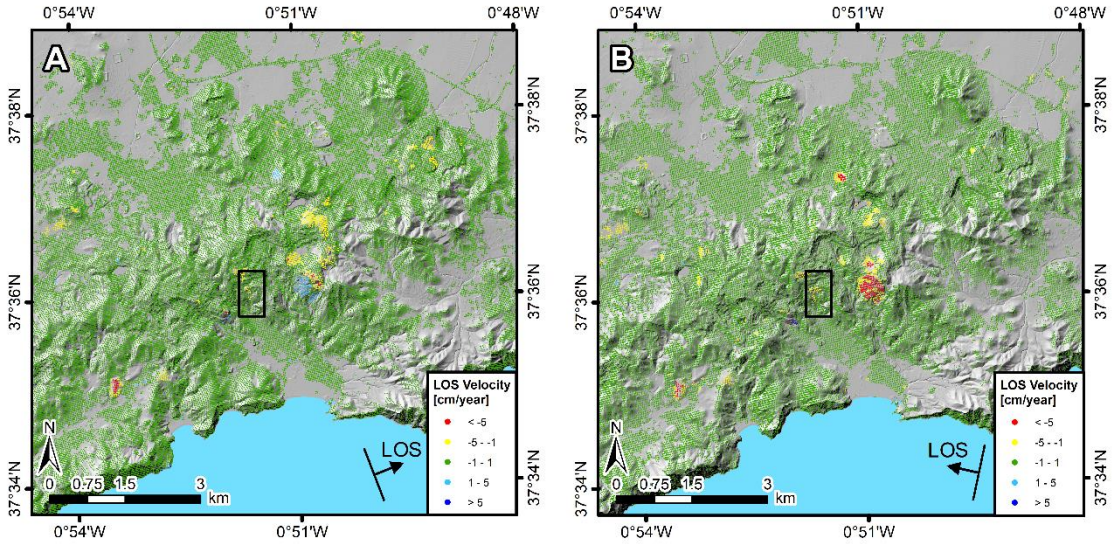

Figure 3. LOS ground velocity maps for the period from 10 July 2017 to 15 November 2018. (**A**) Ascending velocities. (**B**) Descending velocities. The black squares show the location of the slope instability monitored by DGPS and used for the validation analysis.

The results in ascending geometry (Figure 3A) contain 72,610 MPs with a MPs density of 712 MPs/km², whereas the map in descending geometry (Figure 3B) contains 66,293 MPs with a MPs density of 626 MPs/km². Standard deviations of the LOS velocities of all the MPs from the ascending and descending datasets resulted respectively in 0.45 and 0.61 cm/year.

The validation analysis was performed by comparing the InSAR-retrieved LOS velocities with in situ DGPS measurements projected onto the LOS both in ascending and descending geometry (Figure 4). Root mean square error (RMSE) values resulted in 1.06 cm/year and 2.46 cm/year, respectively, for the ascending and descending results (Figure 4F). The difference between both RMSEs is most likely related to the different levels of noise affecting the InSAR data, higher for the descending results according to their standard deviation.

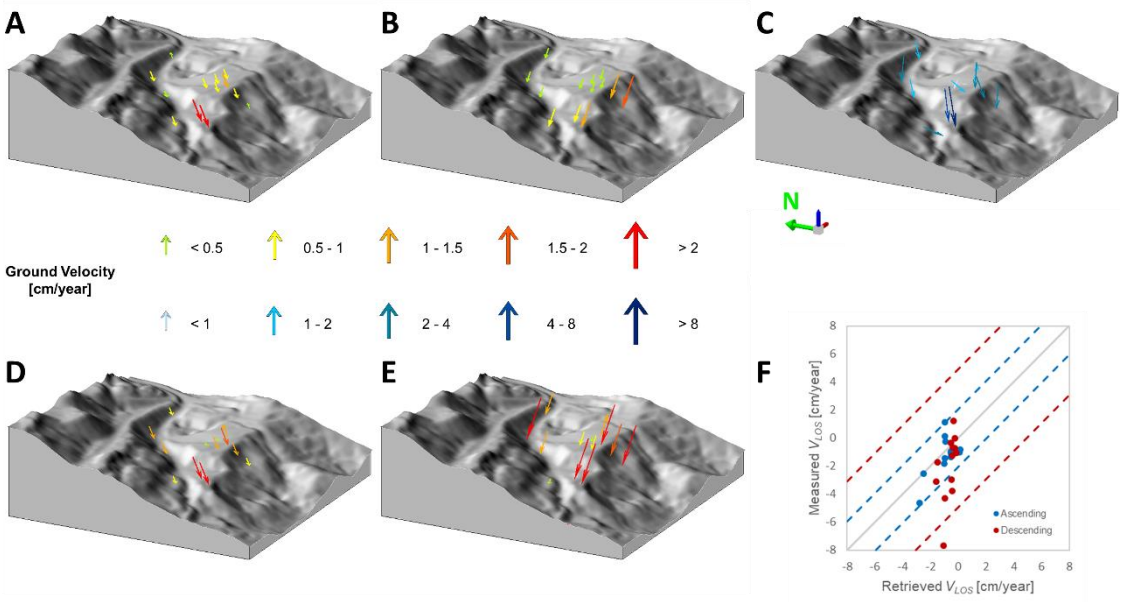

Preprints (www.preprints.org) | NOT PEER-REVIEWED | Posted: 26 April 2021 doi:10.20944/preprints202104.0696.v1

Figure 4. Results of the validation analysis. 3D view of the (**A**) InSAR ascending and (**B**) descending LOS ground velocities over the points monitored by DGPS, (**C**) raw DGPS ground velocities for the period from 11 July 2017 to 15 November 2018, and DGPS ground velocities projected onto the (**D**) ascending and (**E**) descending LOS. (**F**) Scatter plot of the LOS ground velocities V_{LOS} measured by DGPS and retrieved by InSAR. The grey solid line indicates the cases where the retrieved and the measured LOS ground velocities V_{LOS} are exactly equal. The blue (red) dashed lines denote the 95% confidence band for the ascending (descending) data (*i.e.* two times the RMSE).

4.2. Slope unit maps and active deformation slope unit maps

The SUs and ADSUs obtained over the study area showed a high degree of variability for the different combinations of the software r.slopeunits input parameters *a* and *c*. These differences can be observed in detail in Figure 5, for nine of the 56 SU (Figure 5A) and ADSU (Figure 5B) maps obtained over the central part of the study area using different (*a*, *c*) combinations.

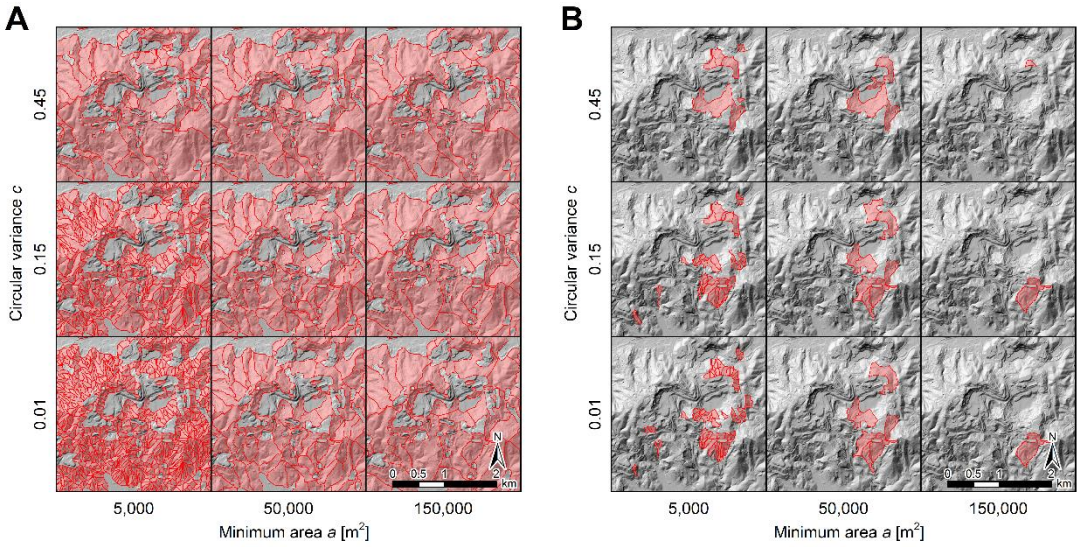

Figure 5. (**A**) Detail of the slope unit (SU) maps obtained with the software r.slopeunits [47] for several combinations of the input parameters *a* and *c*. (**B**) Detail of the active deformation slope unit (ADSU) maps, obtained from the SU maps as described in Section 3.3.

The maximum and minimum number of SUs obtained considering the 56 SU sets resulted in 4,623 and 116 respectively for SU maps 1 (lower left corner in Figure 5A) and 56, for which the mean SU area resulted in 10,000 and 370,000 m², respectively.

The number of ADSUs corresponding to the ADSU sets 1 (lower left corner in Figure 5B) and 56 resulted in 94 and 2, respectively, with a mean ADSU area of 10,000 and 20,000 m², respectively.

Note that when using the finest SU partition, obtained with the smallest values of *a* and *c*, the number of ADSUs more than doubles the number of inventoried landslides. On the other hand, for the coarsest SU partition, a negligible number of ADSUs is obtained. Moreover, in most of the cases using *a* values greater than 150,000 m², no ADSUs were obtained due to the MPs density threshold considered (500 MPs/km²).

In the next section we evaluate the different ADSU sets to find the (*a*, *c*) combination that provides the ADSU set best matching the landslide inventory, *i.e.*, the optimal ADSU set.

4.3. Optimal active deformation slope unit map

The values of the two metrics $F(a, c)$ considered in this work for optimization of the software r.slopeunits input parameters *a* and *c*, Eqs. (5) and (6), are shown in Figure 6. Note that the figure shows the values obtained for the 56 ADSU sets resulting from all the possible (*a*, *c*) combinations. In addition, Figure 7 shows the cumulated frequency size

Preprints (www.preprints.org) | NOT PEER-REVIEWED | Posted: 26 April 2021 doi:10.20944/preprints202104.0696.v1

distributions used to calculate Eq. (6), also for the 56 ADSU sets. For clarity, a few ADSU sets covering the whole range of frequency size distributions are highlighted (Figure 7A). These ADSU sets, denoted by "set 1", "set 3", "set 5", "set 25", "set 27", "set 29", "set 49", "set 51" and "set 53", were obtained with the (*a*, *c*) combinations shown in Figure 5 (from the lower left to the upper right corner). Note that the leftmost point of all distributions is normalized to 100% by definition. The distribution of the inventoried landslides is also depicted (Figure 7B).

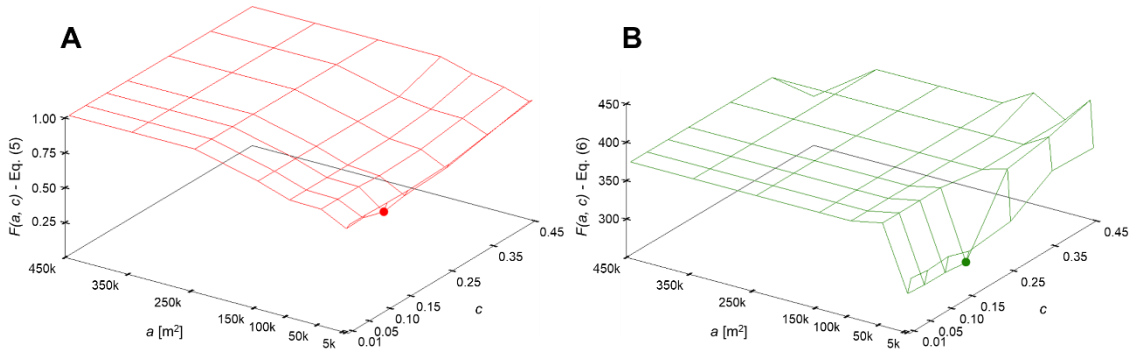

Figure 6. Active deformation slope units (ADSUs) optimization metrics, calculated as a function of the software r.slopeunits [47] input parameters *a* and *c*, for all the possible (*a*, *c*) combinations. (**A**) Values of the metric *F*(*a*, *c*) defined by Eq. (5): the optimal values are found in correspondence with the minimum value of Eq. (5), indicated with a red dot. (**B**) Values of the metric *F*(*a*, *c*) defined by Eq. (6): the minimum value of Eq. (6) is indicated with a green dot.

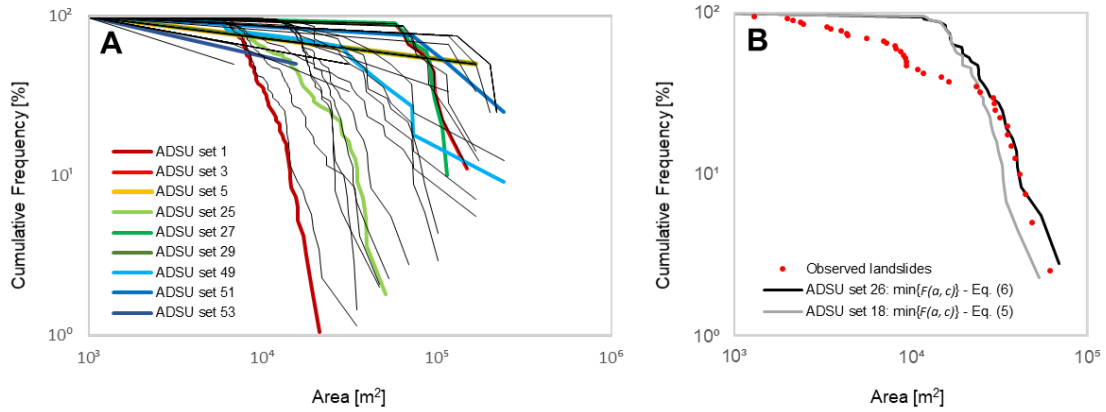

Figure 7. (**A**) Cumulated frequency size distributions of the active deformation slope unit (ADSU) maps for all the possible combinations of the software r.slopeunits [47] input parameters *a* and *c*. The highlighted results are listed and described in the text. (**B**) Cumulated frequency size distributions of the inventoried landslides, the ADSU set corresponding to the minimum value of the metric *F*(*a*, *c*) defined by Eq. (6) (ADSU set 26), and the optimal ADSU set (ADSU set 18), corresponding to the minimum value of the metric *F*(*a*, *c*) defined by Eq. (5).

The results reveal that the higher the value of *a*, the higher the difference between the inventoried landslides and the mapped ADSUs (Figure 6). However, it can be noted that Eq. (5) (Figure 6A) captures a greater variety of results than Eq. (6) (Figure 6B), and increases gradually with increasing values of *a* until reaching *a* = 250,000 m². Starting from that value, the overlap between the mapped ADSUs and the landslide inventory becomes zero, and the error results in a 100%. The set of ADSUs corresponding to the minimum of Eq. (5) (ADSU set 18), shown with a red dot in Figure 6A, was derived from the SU map obtained by (*a*, *c*) = (10,000 m², 0.10). The distribution corresponding to the ADSU set 18 is shown with a grey solid curve in Figure 7B.

On the other hand, if we analyze the results of Eq. (6), we can observe that the values of this metric vary strongly until reaching *a* = 150,000 m². For values above, the results become constant. The reason for this is that several ADSU maps are not comparable with our landslide inventory by using cumulated frequency size distribution plots (Figure 7).

Preprints (www.preprints.org) | NOT PEER-REVIEWED | Posted: 26 April 2021 doi:10.20944/preprints202104.0696.v1

These ADSU maps include few very large ADSUs that do not match the inventoried landslides (*e.g.*, ADSU sets 3, 5, 27, 29, 51 and 53 in Figure 7A). The set of ADSUs corresponding to the minimum of Eq. (6) (ADSU set 26), shown with a green dot in Figure 6B, was derived from the SU map obtained by (a, c) = (10,000 m^2, 0.10). The distribution corresponding to the ADSU set 26 is shown with a black solid curve in Figure 7B.

This means that the metric in Eq. (5) allows a more accurate comparison between the inventory and the ADSU maps, even for maps containing a limited number of ADSUs. For this reason, the optimal ADSU set (ADSU set 18) was selected on the basis of the results obtained from Eq. (5). Note that the (a, c) combination corresponding to the optimal set of ADSUs according to the metric of Eq. (6) (ADSU set 26) is fairly similar to that corresponding to the selected optimal ADSU set (ADSU set 18). In fact, the ADSU set 18 corresponds to the second-best result obtained from Eq. (6) (Figure 7B).

Yet the accuracy, defined as the sum of true positives (TP) and true negatives (TN), is slightly higher for set 18 than for set 26 (99.39% compared to 99.37%) (Table 2). The total false statements are also lower for set 18 (0.62% compared to 0.63%).

Table 2. Confusion matrices and values of the metrics defined by Eq. (5) and (6) for three different outputs: the active deformation areas (ADAs) mapped by means of the so-called ADAFinder software package [29], the active deformation slope unit (ADSU) set 26, corresponding to the minimum value of the metric $F(a, c)$ defined by Eq. (5), and the ADSU set 18 (optimal ADSU set), corresponding to the minimum value of the metric $F(a, c)$ defined by Eq. (5). TN: true negatives. FN: false negatives. FP: false positives. TP: true positives.

	ADA set	**ADSU set 26**	**ADSU set 18**
TN	98.55%	99.11%	99.10%
FN	0.20%	0.24%	0.21%
FP	0.96%	0.39%	0.41%
TP	0.30%	0.26%	0.29%
$F(a, c)$ - Eq. (5)	0.794	0.707	0.679
$F(a, c)$ - Eq. (6)	301.96	291.55	294.55

These results suggest that the metric of Eq. (5) is more appropriate than that in Eq. (6), for the optimization procedure devised in this work. The ADSU maps obtained with both metrics increase the accuracy of the ADAs mapped by ADAFinder (Table 2), which is unable to distinguish slope instabilities from vertical ground movements, by 0.5%. This improvement is also reflected in the values obtained from Eqs. (5) and (6) for the ADSU maps 18 and 26 and for the ADA set (Table 2).

The total number of ADSUs conforming the optimal set (ADSU set 18), resulted in 43 (opaque polygons in Figure 8). In turn, the set of SUs obtained by (a, c) = (10,000 m^2, 0.10), used to derive the optimal ADSU set, was formed by a total of 1,959 SUs. From these 1,959 SUs, 151 were characterized as unknown SUs. This was determined by intersecting the non-active deformation SUs with the two InSAR datasets separately. Those SUs containing less than five MPs both from the ascending and descending datasets, and yielding a density of active MPs (also from the ascending and descending datasets) lower than 500 MPs/km^2, were characterized as unknown SUs (transparent pink polygons in Figure 8). These SUs were mainly located over densely vegetated hillslopes where only few MPs were obtained (SE quadrants in Figures 3A and 3B). No landslides were, however, inventoried over those areas. The remaining 1,756 SUs were characterized as stable SUs (transparent green polygons in Figure 8).

Preprints (www.preprints.org) | NOT PEER-REVIEWED | Posted: 26 April 2021 doi:10.20944/preprints202104.0696.v1

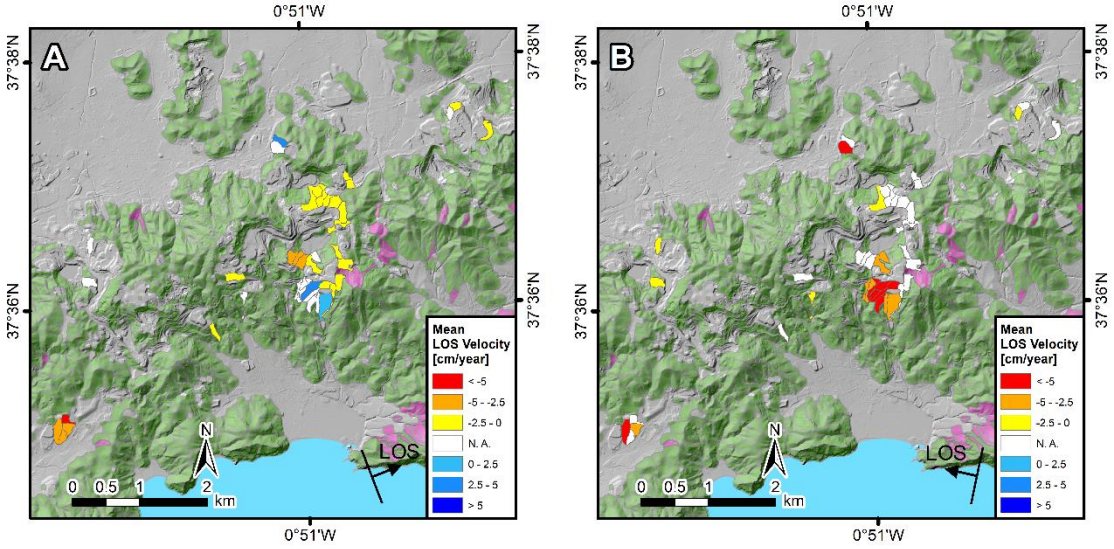

Figure 8. Mean LOS ground velocities obtained for the 43 active deformation slope units (ADSUs) from the optimal set (ADSU set 18). All ADSUs are represented in opaque colors. (**A**) Ascending velocities. (**B**) Descending velocities. ADSUs not detected in each geometry are represented in opaque white. Unknown and stable SUs are also depicted in transparent pink and transparent green respectively.

Mean LOS velocities for the 43 ADSUs from the optimal set both in ascending and descending geometry are respectively presented in Figures 8A and 8B. Note that the 43 ADSUs conforming the optimal set were obtained through the combination of the ascending and descending results. Positive mean LOS velocities in Figure 8 correspond to movement towards the satellite, whereas negative values represent movement away from the satellite. ADSUs not detected in ascending but in descending are represented in opaque white in Figure 8A (and vice versa in Figure 8B).

The number of ADSUs derived using ascending and descending data was 31 and 20, respectively. From among these ADSUs, 10 and 15 presented absolute mean LOS velocities greater than 2.5 cm/year respectively in ascending and descending geometry. These ADSUs can be assimilated to slope instabilities with an absolute degree of confidence, since the maximum RMSE obtained through the validation analysis resulted in 2.46 cm/year.

Positive mean LOS velocities were only obtained in ascending geometry (Figure 8A), for a total of 4 ADSUs. A total of 8 ADSUs were detected in both geometries (ascending and descending). From among them, 3 ADSUs showed opposite direction of movement in ascending and descending, a behavior typically attributed to slope movements having a strong horizontal component. Considering the 43 ADSUs conforming the optimal set—taking maximum absolute values in those ADSUs detected in both geometries, a total of 21 ADSUs presented absolute mean LOS velocities greater than 2.5 cm/year. These 21 ADSUs can therefore be most certainly associated with slope instabilities.

4.4. 2D stability analyses

Out of the 43 ADSUs in the optimal set (ADSU set 18), 14 revealed 2D safety factors *SF*s lower than 1.2, 13 *SF*s between 1.2 and 1.5, and 16 *SF*s greater than 1.5. Only 3 and 5 ADSUs revealed *SF*s lower than 1 and greater than 2, respectively. Most of the ADSUs with *SF*s greater than 2, characterized by very low slope gradients, coincide the southwesternmost cluster of active MPs in Figure 3. 2D landslide sizes *LS*s for the 43 ADSUs ranged from 1,900 to 27,000 m^2.

The median of the aspect was found to offer the best performance for the purpose of obtaining cross-sections. In many cases, however, the differences were not significant—similar results were obtained using the three different aspect values considered (mean, median and mode), indicating a proper delineation result in terms of aspect homogeneity.

Preprints (www.preprints.org) | NOT PEER-REVIEWED | Posted: 26 April 2021 doi:10.20944/preprints202104.0696.v1

Thus, 32.56%, 53.49% and 34.88% of the ADSUs were satisfactorily modeled using the mean, the median and the mode of the aspect, respectively. Concerning the length of the cross-sections, 44.19%, 46.51% and 9.30% of the ADSUs were modeled using 400-, 800- and 1200-m long cross-sections, respectively.

Figure 9 shows detailed results of the 2D stability analyses corresponding to three cross-sections obtained for three particular ADSUs. The cross-sections corresponding to Figures 9A and 9B were obtained using mean aspect values, whereas the cross-section corresponding to Figure 9C was obtained using the median. For convenience, the examples integrate 2D stability analyses performed using 400-, 800- and 1200-m long cross-sections. Note that the slope in Figure 9B corresponds to the slope instability monitored by DGPS (Figure 4).

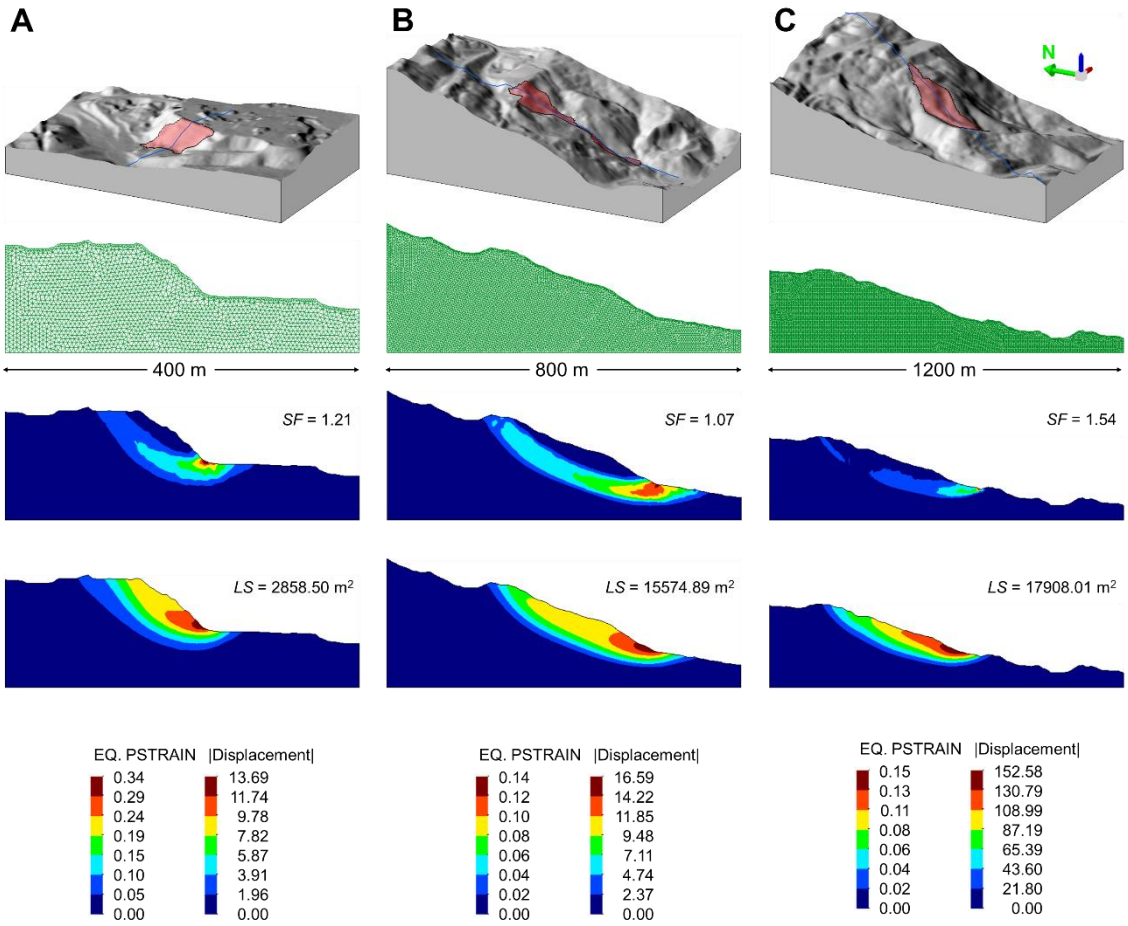

Figure 9. Results of three 2D stability analyses performed using (**A**) 400-, (**B**) 800- and (**C**) 1,200-m long cross-sections derived from three particular active deformation slope units (ADSUs) from the optimal set (ADSU set 18). Fist row: 3D view of the three ADSUs. The blue solid lines represent each profile trace, the 1,200-m long profile trace clipped to the hillshade extent. Second row: finite element meshes corresponding to each profile trace. Third row: equivalent plastic strain contours at failure corresponding to each profile trace. Fourth row: displacement contours (in m) corresponding to each profile trace. The resulting 2D safety factors *SF*s and 2D landslide sizes *LS*s are also presented. The legends for rows third and four are shown at the bottom of the figure.

Eventually, we elaborated two ADSU maps summarizing the results of the 2D stability analyses for the 43 ADSUs from the optimal set (ADSU set 18) (Figure 10). The map in Figure 10A shows the resulting safety factors *SF*s, whereas the map in Figure 10B shows the resulting landslide sizes *LS*s.

Preprints (www.preprints.org) | NOT PEER-REVIEWED | Posted: 26 April 2021 doi:10.20944/preprints202104.0696.v1

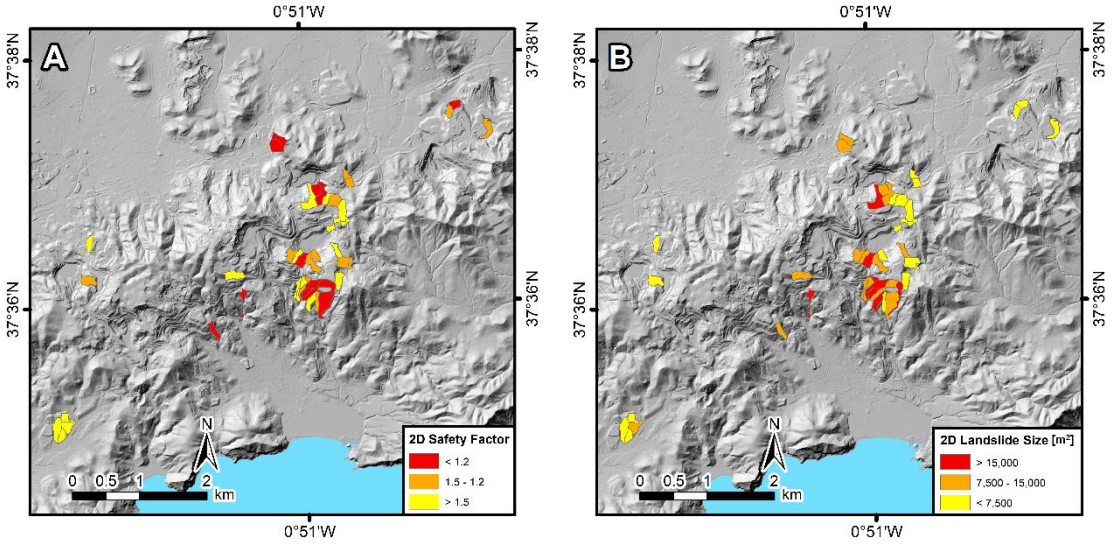

Figure 10. Results of the 2D stability analyses for the 43 active deformation slope units (ADSUs) from the optimal set (ADSU set 18). (**A**) 2D safety factors *SF*s and (**B**) 2D landslide sizes *LS*s.

4. Discussion

This work proposes a new approach for detecting and characterizing slope instabilities at a regional scale, aimed at providing non-expert final users—such as Civil Protection authorities or risk management decision-makers, with easily intelligible products that can thus be exploited for geohazard management purposes. Although the proposed methodology has been applied here to analyze mining-induced slope instabilities, it can likewise be applied to analyze all types of slope instabilities.

Existing approaches for detecting ADAs from InSAR data [29–32] focus on the delineation of the more reliable deforming areas through the aggregation of subsets of points obtained by filtering the raw LOS ground velocity map. Firstly, in order to filter the LOS ground velocity map, these approaches usually select the moving points using an absolute velocity threshold equal to 2σ (two times the standard deviation of the raw LOS ground velocity map). Then, groups of moving points sharing their influence area are aggregated in polygons representing the ADAs.

Given the inability of these approaches to discern between different types of ground movement, sometimes overlapping within a single ADA, it is desirable to develop new approaches that provide further partitioning of the active areas to better analyze ground movements in complex areas with large deformation footprints. In that sense, the ADSU map represents an interesting product that allows a comprehensive analysis of ground movements—in particular, of slope instabilities. Through the aggregation of the moving points within the boundaries of slopes defined by polygons with similar slope-facing direction (aspect), different mean LOS ground velocities can be determined for adjacent partitions. Using the traditional active deformation mapping approaches, such partitions would be integrated into a single polygon, with the consequent loss of information.

Furthermore, in addition to help determining the mean LOS ground velocity of each polygon, SUs can be used to derive numerical modeling geometries, given their high aspect homogeneity. In this work, we devised an automatic procedure to obtain 2D cross-sections for each ADSU and performed simplified stability analyses determining their *SF*s and *LS*s.

The comparison of the computed *SF*s with the maximum absolute mean LOS velocities resulting from the InSAR data (Figure 11) provided interesting results. In principle, these two variables are correlated, assuming that the most unstable slopes should also be the ones showing the highest slope movement rates.

Preprints (www.preprints.org) | NOT PEER-REVIEWED | Posted: 26 April 2021 doi:10.20944/preprints202104.0696.v1

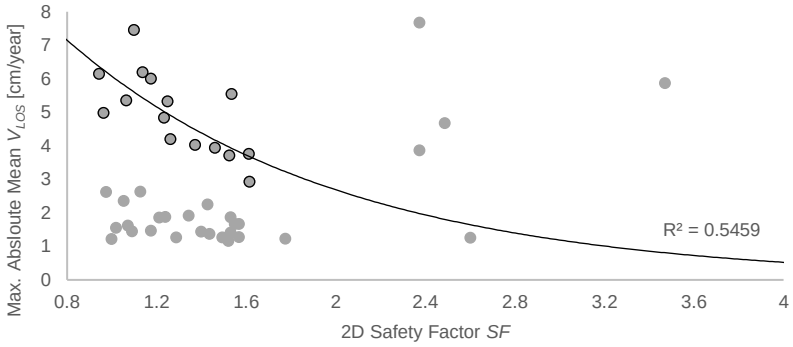

Figure 11. Scatter plot of the maximum absolute mean LOS ground velocities V_{LOS} and the 2D safety factors *SF*s for 15 active deformation slope units (ADSUs) from the optimal set (ADSU set 18). The black curve is a fit of the subset of points outlined in black.

At first glance, if we analyze the scatter plot in Figure 11, we can observe there is no relationship between the two variables in general terms. However, the points are not randomly distributed either. In fact, if we analyze the points exhibiting *SF*s lower than 2, two distinct clusters are found. For one, the group of 21 points with mean LOS velocities of up to 2.5 cm/year, for which there is no relationship between *SF* and mean LOS velocity. Secondly, the group of 17 points with mean LOS velocities greater than 2.5 cm/year, for which a potential relationship between the two variables is observed when excluding the two ADSUs with mean LOS velocities of 2.63 cm/year. Note that the best-fit exponential curve corresponding to those 15 points (black curve in Figure 11) yields a reasonably fair coefficient of determination ($R^2 = 0.55$). Points exhibiting *SF*s greater than 2, which correspond to ADSUs characterized by very low slope gradients, are interpreted as outliers.

This finding is in line with the fact that the maximum RMSE obtained through the validation analysis resulted in 2.46 cm/year. For this reason, the relationship between *SF* and mean LOS velocity is only observed for the ADSUs exhibiting mean LOS velocities greater than 2.5 cm/year—as long as the two ADSUs with mean LOS velocities of 2.63 cm/year, close to 2.5 cm/year, are excluded. ADSUs exhibiting lower velocities cannot be assimilated to slope instabilities with absolute certainty, since they are most likely subjected to errors associated to noisy InSAR data.

These results indicate that significant further efforts are needed in order to improve the relationship between *SF* and mean LOS velocity. Possible solutions for this purpose could include the use of more sophisticated InSAR processing chains providing higher resolution and time series of movement. In the slope stability assessment step, improvement can be the adoption of accurate lithostratigraphic geometry description (considering different materials instead of a single material) and hydrogeological data (instead of assuming fully saturated conditions), possibly with the application of 3D FE modeling.

Although the proposed methodology could be improved by modifying these aspects, it is still useful to generate easy-to-interpret products that can be integrated in the geohazard management chain. In opposition to pixel-based approaches, our methodology provides discrete, easily intelligible results by relying on the assumption that failures cannot be bigger than the physical boundaries of the slopes. By defining the physical boundaries of the slope where the potential failure can occur, the main restriction of pixel-based approaches—related to the lack of correspondence between the landslide size and the pixel size, is overcome.

A further step towards an integrated analysis of slope stability based on these products could be the combination of mean LOS velocities, *SF*s and *LS*s into a hazard proxy. According to probabilistic models for landslide hazard assessment, landslide hazard is the probability of occurrence within a specified period and within a given area of a landslide of a given magnitude [61]. Assuming independence among the three probabilities, the landslide hazard can be defined as follows [62]:

Preprints (www.preprints.org) | NOT PEER-REVIEWED | Posted: 26 April 2021 doi:10.20944/preprints202104.0696.v1

$$H_L = P(A_L) \cdot P(N_L) \cdot S, \quad (7)$$

where $P(A_L)$, $P(N_L)$ and S are respectively the probability of landslide size (magnitude), of landslide occurrence in an established period (frequency), and of landslide spatial occurrence (susceptibility), given the local environmental setting.

Here, rather than opting for a quantitative probabilistic analysis of the landslide hazard, we adopted a qualitative approach to derive a hazard proxy taking into account the results of the methodology (*i.e.*, mean LOS velocities, *SF*s and *LS*s), obtained however on a deterministic basis. The slope instability hazard proxy was evaluated by combining the *LS* as a proxy for magnitude, the mean LOS velocity as a proxy for frequency, and the *SF* as a proxy for susceptibility (Figure 12). For each combination, the degree of hazard was established and expressed in qualitative terms. Figure 12A shows the maximum absolute mean LOS velocities resulting from the InSAR data. The measuring direction, indicating whether the values correspond to ascending or descending data, is also depicted. The matrix defined to evaluate the slope instability hazard proxy is shown in Figure 12C.

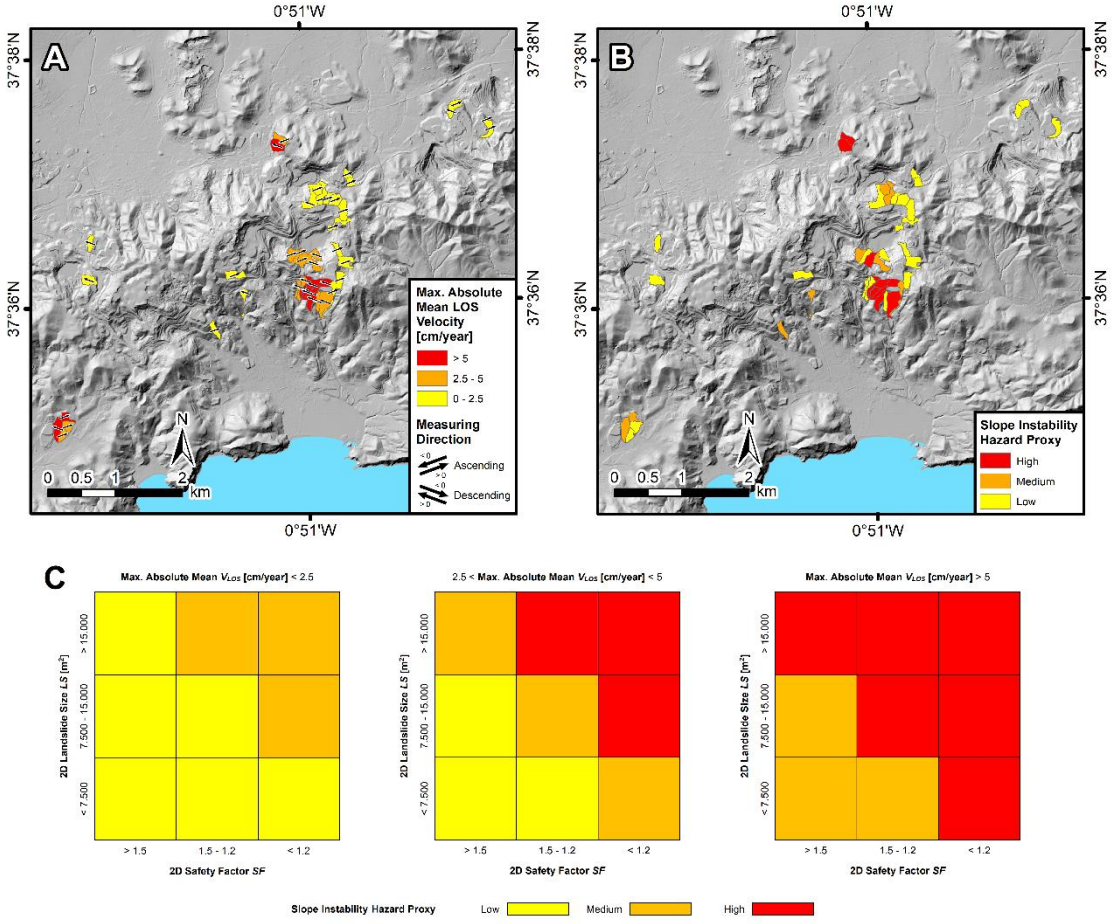

Figure 12. (**A**) Maximum absolute mean LOS ground velocities for the 43 active deformation slope units (ADSUs) from the optimal set (ADSU set 18). Directions of movement are also indicated. (**B**) Slope instability hazard proxy obtained through the combination of the 2D landslide size *LS* (as a proxy for magnitude of failure), the LOS ground velocity V_{LOS} (as a proxy for frequency of failure) and the 2D safety factor *SF* (as a proxy for susceptibility of failure) for each ADSU. (**C**) Matrix defined to evaluate the slope instability hazard proxy.

The main drawback of this analysis is the oversimplification of both the geotechnical setting and the groundwater pore-water pressure distribution, as well as the introduction of a time frame based on the mean LOS velocity. The resulting hazard proxy should therefore only be used to act as a trigger for more detailed geotechnical assessment of the identified priority areas. In contrast, this simplicity allows the approach to be fully scalable.

Preprints (www.preprints.org) | NOT PEER-REVIEWED | Posted: 26 April 2021 doi:10.20944/preprints202104.0696.v1

This last point is particularly interesting when considering that massive InSAR data will shortly be available thanks to upcoming projects such as the Copernicus European Ground Motion Service. Once the open-access InSAR data to be provided by this project all over Europe will be available, it will be possible to perform slope stability analysis over all mining waste disposal areas at a European scale using the proposed methodology.

To illustrate this point, we elaborated an SU map over the Region of Murcia focusing exclusively on mining and waste disposal areas (Figure 13). For this purpose, we extracted the mineral extraction areas and dump sites from the Corine Land Cover 2018 [63]. Note that the map only contains SUs that overlap these two land cover classes (Figure 13B). The SUs were delineated with the software r.slopeunits [47] excluding all areas with slope gradient lower than 5^0 and using the optimal values of the input parameters a and c we obtained for Sierra Minera—*i.e.* (a, c) = (10,000 m², 0.10).

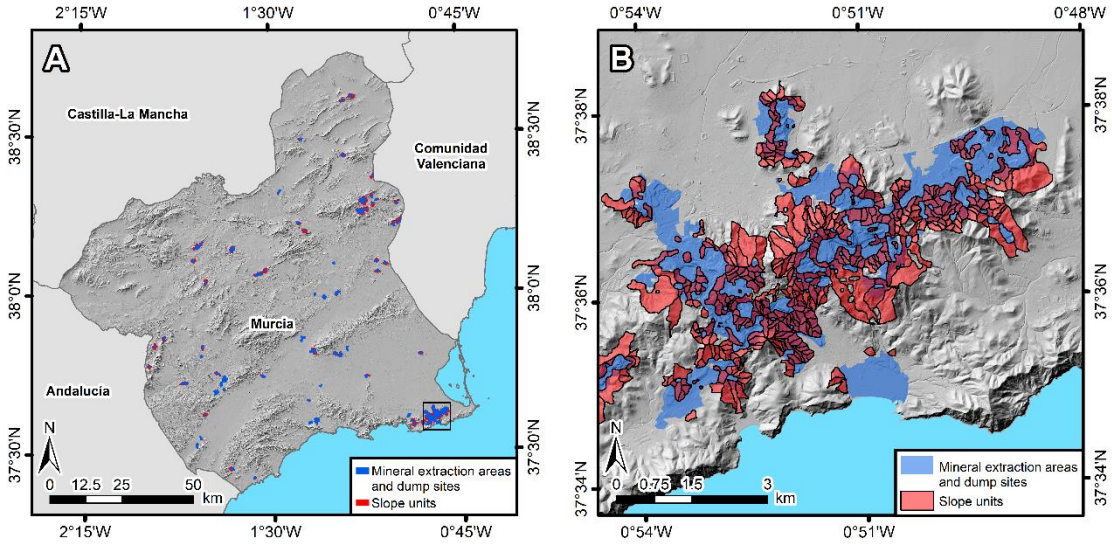

Figure 13. (**A**) Mineral extraction areas and dump sites extracted from the Corine Land Cover 2018 [63] over the Region of Murcia, and slope units (SUs) overlapping both classes, obtained with the software r.slopeunits [47] using the optimal values of the input parameters a and c, *i.e.* (a, c) = (10,000 m², 0.10). The black square shows the location of the study area. (**B**) Detail of the mineral extraction areas and dump sites over the study area, and slope units (SUs) intersecting both classes.

5. Conclusions

This paper introduces a novel methodology for regional slope stability analysis in mining waste disposal areas. The methodology combines satellite InSAR, SUs and 2D FE modeling to quantify mean LOS velocities, *SF*s and *LS*s for a set of slope instabilities derived following a semi-automatic procedure.

The first step of the methodology is to generate LOS ground velocity maps through InSAR processing, which must be properly validated. The second step consists in the aggregation of the moving points within the boundaries of morphological SUs, which allows to obtain an ADSU map optimized with respect to the landslide inventory. The last step is to perform stability analyses on each of the ADSUs within the optimal map.

In this work, InSAR processing was carried out by using the unsupervised FASTVEL processing chain [12,40], its results validated using in situ DGPS data. For SU delineation and 2D FE modeling, we used the software r.slopeunits [47] and the GeHoMadrid code [59,60], respectively.

The methodology, has been set up for Sierra Minera (Murcia), a former mining area in southeast Spain, where it has proven effective to detect and characterize a considerably large number of slope instabilities. Out of the 1,959 SUs used to derive the optimal ADSU set, a total of 43 were found to be active according to the InSAR data, whereas 1,756 were found to be stable. Only 151 SUs, located in areas poorly covered by the InSAR data, were characterized as unknown. A total of 21 out of the 43 ADSUs conforming the optimal

 doi:10.20944/preprints202104.0696.v1

ADSU set presented absolute mean LOS velocities greater than 2.5 cm/year. These 21 ADSUs can be assimilated to slope instabilities with absolute certainty considering that the maximum RMSE obtained through the validation analysis resulted in 2.46 cm/year. The set of SUs used to derive the optimal ADSU set was obtained by (a, c) = (10,000 m², 0.10).

From among the 43 ADSUs conforming the optimal ADSU set, 14 of them revealed *SF*s lower than 1.2, 13 of them *SF*s between 1.2 and 1.5, and 16 of them *SF*s greater than 1.5. Only 5 ADSUs characterized by very low slope gradients, revealed *SF*s greater than 2. *LS*s for the 43 ADSUs ranged from 1,900 to 27,000 m².

The comparison of the computed *SF*s with the maximum absolute mean LOS velocities resulting from the InSAR data led to noteworthy observations. The best-fit exponential curve obtained for 15 ADSUs presenting *SF*s lower than 2 and mean LOS velocities greater than 2.5 cm/year, yielded a reasonably fair coefficient of determination ($R^2 = 0.55$), indicating a potential relationship between *SF* and mean LOS velocity. These finding is consistent with the maximum RMSE obtained through the validation analysis (2.46 cm/year). However, the relationship between *SF* and mean LOS velocity, was not observed for two ADSUs with mean LOS velocities of 2.63 cm/year, still close to 2.46 cm/year.

Possible improvements to further refine these results could include the use of more sophisticated InSAR processing chains providing LOS ground velocity maps at full resolution and time series of movement, the adoption of precise lithostratigraphic and hydrogeological data in the stability analyses, and the application of 3D FE modeling.

This paper presents the first study using FASTVEL for slope stability mapping, and providing validation results for FASTVEL. It also provides a new systematic, automatic procedure based on SUs delineation to aggregate InSAR data, and reports for the first time the use of SUs to automatically derive 2D FE modeling geometries. Furthermore, this work discusses the possibility of evaluating the slope instability hazard through a qualitative approach combining the results of the methodology (*i.e.* mean LOS velocities, *SF*s and *LS*s) to derive a hazard proxy.

It should be noted that the results of the proposed methodology can be periodically updated for continuous evaluation by performing the analyses on a regular basis. The application of the methodology allows to generate products that provide non-expert end users with intelligible, clear and easily comparable information that can be integrated in the geohazard management chain. These products can thus be exploited by Civil Protection or risk management authorities for geohazard management purposes. Moreover, since the methodology is fully scalable, its application for slope stability analysis in all European mining waste disposal areas will soon be possible, once the oncoming massive InSAR data to be provided by ongoing projects such as the Copernicus European Ground Motion Service will be available. Although the methodology was applied here to analyze mining-related slope instabilities, it can likewise be used to analyze slope instabilities affecting natural and man-made slopes in general.

Author Contributions: Conceptualization, J.L.-V., J.A.F.-M. and G.H.; methodology, J.L.-V., J.A.F.-M. and G.H.; software, J.L.-V., J.A.F.-M., A.B. and M.A.; validation, J.L.-V. and J.C.G.-D.; formal analysis, P.E. and A.B.; investigation, J.C.G.-D. and R.S.; resources, P.E. and A.B.; data curation, C.R.-C., J.A.N. and V.K.; funding acquisition, R.S. and G.H.; project administration, G.H.; supervision, J.A.F.-M. and M.A.; visualization, J.L.-V and P.E..; writing—original draft preparation, J.L.-V., J.A.F.-M. and G.H.; writing—review and editing, all authors. All authors have read and agreed to the published version of the manuscript.

Funding: This work has received funding from the Regional Administration of Madrid (Comunidad de Madrid) in the framework of the Industrial PhD Project GEODRON (IND2017/AMB-7789).

Data Availability Statement: The data presented in this study are available at IGME on request from the corresponding author.

Acknowledgments: First author shows gratitude for the working contract arranged with HEMAV SL for the development of the Industrial PhD Project GEODRON. Copernicus Sentinel-1 IW SAR data were provided via and processed in ESA's Geohazards Exploitation Platform (GEP), in the framework of the GEP Early Adopters Programme 2015–2020 and the Geohazards Lab initiative,

the latter developed under the CEOS Working Group on Disasters. Data processing was carried out with the FASTVEL service developed and integrated by TRE ALTAMIRA in the GEP. The authors thank the whole GEP Team for providing technical support and assistance to use the platform, and TRE ALTAMIRA for making the FASTVEL chain available.

Conflicts of Interest: The authors declare no conflict of interest.

References

1. Brown, E.T. Underground Excavations in Rock. *Undergr. Excav. Rock* **1980**, doi:10.1201/9781482288926.
2. Botin, J.A. *Sustainable Management of Mining Operations*; 2009; ISBN 978-0-87335-267-3.
3. Bell, F.G.; Stacey, T.R.; Genske, D.D. Mining subsidence and its effect in the environment: Some differing examples. *Environ. Geol.* **2000**, *40*, 135–152, doi:10.1007/s002540000140.
4. Osasan, K.S.; Afeni, T.B. Review of surface mine slope monitoring techniques. *J. Min. Sci.* **2010**, *46*, 177–186, doi:10.1007/s10913-010-0023-8.
5. O'Connor, K.M.; Murphy, E.W. TDR monitoring as a component of subsidence risk assessment. *Int. J. rock Mech. Min. Sci. Geomech. Abstr.* **1997**, *34*, 619, doi:10.1016/S1365-1609(97)00134-2.
6. Zhou, D.; Wu, K.; Chen, R.; Li, L. GPS/terrestrial 3D laser scanner combined monitoring technology for coal mining subsidence: A case study of a coal mining area in Hebei, China. *Nat. Hazards* **2014**, *70*, 1197–1208, doi:10.1007/s11069-013-0868-7.
7. Carlà, T.; Farina, P.; Intrieri, E.; Ketizmen, H.; Casagli, N. Integration of ground-based radar and satellite InSAR data for the analysis of an unexpected slope failure in an open-pit mine. *Eng. Geol.* **2018**, *235*, 39–52, doi:10.1016/j.enggeo.2018.01.021.
8. Dick, G.J.; Eberhardt, E.; Cabrejo-Liévano, A.G.; Stead, D.; Rose, N.D. Development of an early-warning time-of-failure analysis methodology for open-pit mine slopes utilizing ground-based slope stability radar monitoring data. *Can. Geotech. J.* **2015**, *52*, 515–529, doi:10.1139/cgj-2014-0028.
9. Osasan, K.S.; Stacey, T.R. Automatic prediction of time to failure of open pit mine slopes based on radar monitoring and inverse velocity method. *Int. J. Min. Sci. Technol.* **2014**, *24*, 275–280, doi:10.1016/j.ijmst.2014.01.021.
10. Francioni, M.; Salvini, R.; Stead, D.; Giovannini, R.; Riccucci, S.; Vanneschi, C.; Gullì, D. An integrated remote sensing-GIS approach for the analysis of an open pit in the Carrara marble district, Italy: Slope stability assessment through kinematic and numerical methods. *Comput. Geotech.* **2015**, *67*, 46–63, doi:10.1016/j.compgeo.2015.02.009.
11. Tong, X.; Liu, X.; Chen, P.; Liu, S.; Luan, K.; Li, L.; Liu, S.; Liu, X.; Xie, H.; Jin, Y.; et al. Integration of UAV-based photogrammetry and terrestrial laser scanning for the three-dimensional mapping and monitoring of open-pit mine areas. *Remote Sens.* **2015**, *7*, 6635–6662, doi:10.3390/rs70606635.
12. Ferretti, A.; Prati, C.; Rocca, F. Permanent scatterers in SAR interferometry. *IEEE Trans. Geosci. Remote Sens.* **2001**, *39*, 8–20, doi:10.1109/36.898661.
13. Ng, A.H.M.; Ge, L.; Yan, Y.; Li, X.; Chang, H.C.; Zhang, K.; Rizos, C. Mapping accumulated mine subsidence using small stack of SAR differential interferograms in the Southern coalfield of New South Wales, Australia. *Eng. Geol.* **2010**, *115*, 1–15, doi:10.1016/j.enggeo.2010.07.004.
14. Styles, T..; Stead, D.; Eberhardt, E.; Rabus, B.; Gaida, M.; Bloom, J. Integrated Numerical Modelling and Insar Monitoring of a Slow Moving Slope Instability at Bingham Canyon Mine. *Slope Stab. 2011 Int. Symp. Rock Slope Stab. Open Pit Min. Civ. Eng.* **2011**.
15. Woo, K.S.; Eberhardt, E.; Rabus, B.; Stead, D.; Vyazmensky, A. Integration of field characterisation, mine production and InSAR monitoring data to constrain and calibrate 3-D numerical modelling of block caving-induced subsidence. *Int. J. Rock Mech. Min. Sci.* **2012**, *53*, 166–178, doi:10.1016/j.ijrmms.2012.05.008.
16. Alex, H.M.N.G.; Linlin, G.E.; Zhang, K.; Chang, H.C.; Li, X.; Rizos, C.; Omura, M. Deformation mapping in three dimensions for underground mining using InSAR - Southern highland coalfield in New South Wales, Australia. *Int. J.*

Remote Sens. **2011**, *32*, 7227–7256, doi:10.1080/01431161.2010.519741.

17. Samsonov, S.; d'Oreye, N.; Smets, B. Ground deformation associated with post-mining activity at the French-German border revealed by novel InSAR time series method. *Int. J. Appl. Earth Obs. Geoinf.* **2013**, *23*, 142–154, doi:10.1016/j.jag.2012.12.008.
18. Zhao, C.; Lu, Z.; Zhang, Q. Time-series deformation monitoring over mining regions with SAR intensity-based offset measurements. *Remote Sens. Lett.* **2013**, *4*, 436–445, doi:10.1080/2150704X.2012.746482.
19. Carlà, T.; Intrieri, E.; Raspini, F.; Bardi, F.; Farina, P.; Ferretti, A.; Colombo, D.; Novali, F.; Casagli, N. Perspectives on the prediction of catastrophic slope failures from satellite InSAR. *Sci. Rep.* **2019**, *9*, doi:10.1038/s41598-019-50792-y.
20. Thomas, A.; Edwards, S.; Engels, J.; Mccormack, H.; Hopkins, V.; Holley, R. Earth observation data and satellite InSAR for the remote monitoring of tailings storage facilities: a case study of Cadia Mine, Australia. *Proc. 22nd Int. Conf. Paste, Thick. Filtered Tailings* **2019**, 183–195, doi:10.36487/acg_rep/1910_11_thomas.
21. Paradella, W.R.; Ferretti, A.; Mura, J.C.; Colombo, D.; Gama, F.F.; Tamburini, A.; Santos, A.R.; Novali, F.; Galo, M.; Camargo, P.O.; et al. Mapping surface deformation in open pit iron mines of Carajás Province (Amazon Region) using an integrated SAR analysis. *Eng. Geol.* **2015**, *193*, 61–78, doi:10.1016/j.enggeo.2015.04.015.
22. Holden, D.; Donegan, S.; Pon, A. Brumadinho Dam InSAR study: analysis of TerraSAR-X, COSMO-SkyMed and Sentinel-1 images preceding the collapse. **2020**, 293–306, doi:10.36487/acg_repo/2025_15.
23. Herrera, G.; Tomás, R.; Vicente, F.; Lopez-Sanchez, J.M.; Mallorquí, J.J.; Mulas, J. Mapping ground movements in open pit mining areas using differential SAR interferometry. *Int. J. Rock Mech. Min. Sci.* **2010**, *47*, 1114–1125, doi:10.1016/j.ijrmms.2010.07.006.
24. López-Vinielles, J.; Ezquerro, P.; Fernández-Merodo, J.A.; Béjar-Pizarro, M.; Monserrat, O.; Barra, A.; Blanco, P.; García-Robles, J.; Filatov, A.; García-Davalillo, J.C.; et al. Remote analysis of an open-pit slope failure: Las Cruces case study, Spain. *Landslides* **2020**, 1–16, doi:10.1007/s10346-020-01413-7.
25. Williams, C.; Ross, B.; Zebker, M.; Gaida, M.; Morkeh, J.; Robotham, M.E. Assessment of historic InSAR monitoring data prior to the Manefay Slide at the Bingham Canyon Mine using the latest analytical techniques. *53rd U.S. Rock Mech. Symp.* **2019**.
26. Herrera, G.; Tomás, R.; Lopez-Sanchez, J.M.; Delgado, J.; Mallorqui, J.J.; Duque, S.; Mulas, J. Advanced DInSAR analysis on mining areas: La Union case study (Murcia, SE Spain). *Eng. Geol.* **2007**, *90*, 148–159, doi:10.1016/j.enggeo.2007.01.001.
27. Herrera, G.; Álvarez Fernández, M.I.; Tomás, R.; González-Nicieza, C.; López-Sánchez, J.M.; Álvarez Vigil, A.E. Forensic analysis of buildings affected by mining subsidence based on Differential Interferometry (Part III). *Eng. Fail. Anal.* **2012**, *24*, 67–76, doi:10.1016/j.engfailanal.2012.03.003.
28. Instituto Geológico y Minero de España. *Estudio geotécnico para el depósito de residuos de la bahía de Portman en corta minera*; Madrid; Unpublished report, 1996;
29. Barra, A.; Solari, L.; Béjar-Pizarro, M.; Monserrat, O.; Bianchini, S.; Herrera, G.; Crosetto, M.; Sarro, R.; González-Alonso, E.; Mateos, R.M.; et al. A methodology to detect and update active deformation areas based on Sentinel-1 SAR images. *Remote Sens.* **2017**, *9*, 1–19, doi:10.3390/rs9101002.
30. Tomás, R.; Pagán, J.I.; Navarro, J.A.; Cano, M.; Luis Pastor, J.; Riquelme, A.; Cuevas-González, M.; Crosetto, M.; Barra, A.; Monserrat, O.; et al. Semi-Automatic Identification and Pre-Screening of Geological-Geotechnical Deformational Processes Using Persistent Scatterer Interferometry Datasets. *mdpi.com* **2019**, *11*, 1675, doi:10.3390/rs11141675.
31. Navarro, J.A.; Cuevas, M.; Tomás, R.; Barra, A.; Crosetto, M. A toolset to detect and classify active deformation areas using interferometric SAR data. *GISTAM 2019 - Proc. 5th Int. Conf. Geogr. Inf. Syst. Theory, Appl. Manag.* **2019**, 167–174, doi:10.5220/0007617701670174.
32. Navarro, J.A.; Tomás, R.; Barra, A.; Pagán, J.I.; Reyes-Carmona, C.; Solari, L.; Vinielles, J.L.; Falco, S.; Crosetto, M. ADAtools: Automatic detection and classification of active deformation areas from PSI displacement maps. *ISPRS Int. J.*

Geo-Information **2020**, *9*, 584, doi:10.3390/ijgi9100584.

33. Manteca, J.; Ovejero, G. Los yacimientos Zn, Pb, Ag-Fe del distrito minero de la La Unión-Cartagena, Bética Oriental. 1992.
34. Conesa, H.M.; Schulin, R.; Nowack, B. Mining landscape: A cultural tourist opportunity or an environmental problem? The study case of the Cartagena-La Unión Mining District (SE Spain). *Ecol. Econ.* **2008**, *64*, 690–700, doi:10.1016/j.ecolecon.2007.06.023.
35. Sanz De Galdeano, C.; Vera, J.A. Stratigraphic record and palaeogeographical context of the Neogene basins in the Betic Cordillera, Spain. *Basin Res.* **1992**, *4*, 21–36, doi:10.1111/j.1365-2117.1992.tb00040.x.
36. Robles-Arenas, V.M.; Rodríguez, R.; García, C.; Manteca, J.I.; Candela, L. Sulphide-mining impacts in the physical environment: Sierra de Cartagena-La Unión (SE Spain) case study. *Environ. Geol.* **2006**, *51*, 47–64, doi:10.1007/s00254-006-0303-4.
37. Gomez-Ros, J.M.; Garcia, G.; Peñas, J.M. Assessment of restoration success of former metal mining areas after 30 years in a highly polluted Mediterranean mining area: Cartagena-La Unión. *Ecol. Eng.* **2013**, *57*, 393–402, doi:10.1016/j.ecoleng.2013.04.044.
38. Cruden, D.; Varnes, D. Landslides: Investigation and Mitigation. Chapter 3 - Landslide Types and Processes. *Transp. Res. Board Spec. Rep.* **1996**.
39. Instituto Geográfico Nacional Centro de Descargas del CNIG 2019.
40. Berardino, P.; Fornaro, G.; Lanari, R.; Sansosti, E. A new algorithm for surface deformation monitoring based on small baseline differential SAR interferograms. *IEEE Trans. Geosci. Remote Sens.* **2002**, doi:10.1109/TGRS.2002.803792.
41. Iglesias, R.; Blanco, P.; Ordoqui, P.; Lopez, A.; Balague, X.; Gili, A.; Bianchi, M.; Monells, D. FASTVEL: a PSI GEP service for terrain motion velocity map generation. In Proceedings of the Fringe 2017 Workshop; APA, 2017; p. 109.
42. Galve, J.P.; Pérez-Peña, J.V.; Azañón, J.M.; Closson, D.; Caló, F.; Reyes-Carmona, C.; Jabaloy, A.; Ruano, P.; Mateos, R.M.; Notti, D.; et al. Evaluation of the SBAS InSAR service of the European space Agency's Geohazard Exploitation Platform (GEP). *Remote Sens.* **2017**, *9*, doi:10.3390/rs9121291.
43. Foumelis, M.; Papadopoulou, T.; Bally, P.; Pacini, F.; Provost, F.; Patruno, J. Monitoring Geohazards Using On-Demand and Systematic Services on Esa's Geohazards Exploitation Platform. *Int. Geosci. Remote Sens. Symp.* **2019**, 5457–5460, doi:10.1109/IGARSS.2019.8898304.
44. Terradue FASTVEL for displacement velocity map generation Available online: https://docs.terradue.com/geohazards-tep/tutorials/fastvel.html (accessed on Dec 1, 2020).
45. Carrara, A.; Cardinali, M.; Guzzetti, F. Uncertainty in assessing landslide hazard and risk. *ITC J.* **1992**, *1992–2*, 172–183.
46. Guzzetti, F.; Carrara, A.; Cardinali, M.; Reichenbach, P. Landslide hazard evaluation: A review of current techniques and their application in a multi-scale study, Central Italy. *Geomorphology* **1999**, *31*, 181–216, doi:10.1016/S0169-555X(99)00078-1.
47. Alvioli, M.; Marchesini, I.; Reichenbach, P.; Rossi, M.; Ardizzone, F.; Fiorucci, F.; Guzzetti, F. Automatic delineation of geomorphological slope units with r.slopeunits v1.0 and their optimization for landslide susceptibility modeling. *Geosci. Model Dev.* **2016**, *9*, 3975–3991, doi:10.5194/gmd-9-3975-2016.
48. Alvioli, M.; Guzzetti, F.; Marchesini, I. Parameter-free delineation of slope units and terrain subdivision of Italy. *Geomorphology* **2020**, *358*, doi:10.1016/j.geomorph.2020.107124.
49. Hansen, A. Landslide hazard analysis. *Slope Instab.* **1984**, 523–602.
50. Carrara, A.; Cardinali, M.; Detti, R.; Guzzetti, F.; Pasqui, V.; Reichenbach, P. GIS techniques and statistical models in evaluating landslide hazard. *Earth Surf. Process. Landforms* **1991**, *16*, 427–445, doi:10.1002/esp.3290160505.
51. Carrara, A.; Cardinali, M.; Guzzetti, F.; Reichenbach, P. Gis Technology in Mapping Landslide Hazard. In; Springer, Dordrecht, 1995; pp. 135–175.
52. Guzzetti, F.; Galli, M.; Reichenbach, P.; Ardizzone, F.; Cardinali, M. *Landslide hazard assessment in the Collazzone area, Umbria, Central Italy Natural Hazards and Earth System Sciences Landslide hazard assessment in the Collazzone area, Umbria, Central Italy*;

2006; Vol. 6;.

53. Guzzetti, F.; Cardinali, M.; Reichenbach, P. Comparing Landslide Maps: A Case Study in the Upper Tiber River Basin, Central Italy. *Environ. Manage.* **2000**, *25*, 247–263, doi:10.1007/s002679910020.
54. Alvioli, M.; Mondini, A.C.; Fiorucci, F.; Cardinali, M.; Marchesini, I. Topography-driven satellite imagery analysis for landslide mapping. *Geomatics, Nat. Hazards Risk* **2018**, *9*, 544–567, doi:10.1080/19475705.2018.1458050.
55. Domènech, G.; Alvioli, M.; Corominas, J. Preparing first-time slope failures hazard maps: from pixel-based to slope unit-based. *Landslides* **2020**, *17*, 249–265, doi:10.1007/s10346-019-01279-4.
56. Domènech, G. Assessment of the magnitude-frequency relationship of landslides and rockfalls: Application to hazard mapping, Dissertation, Universitat Politècnica de Catalunya, 2015.
57. Zienkiewicz, O.C.; Humpheson, C.; Lewis, R.W. Associated and non-associated visco-plasticity and plasticity in soil mechanics. *Geotechnique* **1975**, doi:10.1680/geot.1975.25.4.671.
58. Dawson, E.M.; Roth, W.H.; Drescher, A. Slope stability analysis by strength reduction. *Geotechnique* **1999**, doi:10.1680/geot.1999.49.6.835.
59. Fernández-Merodo, J.A. Une approche à la modélisation des glissements et des effondrements de terrains: Initiation et propagation, Dissertation, École Centrale Paris, 2001.
60. Mira, P. Análisis por Elementos Finitos de Problemas de Rotura de Geomateriales, Dissertation, Universidad Politécnica de Madrid, 2002.
61. Alvioli, M.; Melillo, M.; Guzzetti, F.; Rossi, M.; Palazzi, E.; von Hardenberg, J.; Brunetti, M.T.; Peruccacci, S. Implications of climate change on landslide hazard in Central Italy. *Sci. Total Environ.* **2018**, *630*, 1528–1543, doi:10.1016/j.scitotenv.2018.02.315.
62. Guzzetti, F. Landslide hazard and risk assessment, Dissertation, Rheinische Friedrich-Wilhelms-Universität Bonn, 2006.
63. Copernicus Land Monitoring Corine Land Cover (CLC) 2018 Version 2020_20u1 Available online: https://land.copernicus.eu/pan-european/corine-land-cover/clc2018.